RSC Advances

PAPER

Cite this: *RSC Adv.*, 2022, **12**, 30577

Visible-light photoelectrocatalysis/H_2O_2 synergistic degradation of organic pollutants by a magnetic Fe_3O_4@SiO_2@mesoporous TiO_2 catalyst-loaded photoelectrode†

Bo Zhang, Xuemei Li, * Yongshan Ma, Tianyi Jiang, Yanyan Zhu and Huixue Ren

Received 18th August 2022
Accepted 21st October 2022

DOI: 10.1039/d2ra05183d

rsc.li/rsc-advances

In this paper, we describe a method for photoelectrocatalysis (PEC)/H_2O_2 synergistic degradation of organic pollutants with a magnetic Fe_3O_4@SiO_2@mesoporous TiO_2 (FST) photocatalyst-loaded electrode. At optimal conditions of pH 3.0, 2.25% H_2O_2, working electrode (fixed FST 30 mg) potential +0.6 V (*vs.* SCE), and 10 mg L^{-1} of all experimental pollutants, the FST PEC/H_2O_2 synergistic system exhibited high activity and stability for the removal of various organic pollutants under visible light with comparable degradation efficiencies, including MB (98.8%), rhodamine B (Rh B, 96.7%), methyl orange (MO, 97.7%), amoxicillin (AMX, 83.9%). Moreover, this system obtained TOC removal ratios of 83.5% (MB), 77.9% (Rh B), 80.2% (MO), 65.5% (AMX) within 8 min. The kinetic rate constants of the PEC/H_2O_2 synergistic system were nearly 53 and 1436 times higher than that of the PEC process and H_2O_2 photolysis under visible light, respectively. Furthermore, the main reactive oxidant species ($^{\bullet}OH$, $^{\bullet}O_2^-$) were studied and enhanced mechanisms of the photocatalytic-electro-H_2O_2 coupling system were proposed. This work brings new insights to efficiently purify organic pollutants by PEC coupled with peroxide under solar light illumination.

1. Introduction

With advances in industrialization and rapid population growth, organic pollutants are frequently detected in water environments. They continue to be enriched in food chains and food webs, endangering ecological environments and human health.[1] These organic pollutants cannot be completely eliminated by wastewater treatment processes, resulting in residues in groundwater and surface water. Therefore, it is necessary to develop suitable technological approaches for the decomposition and mineralization of refractory organic pollutants and removal of refractory organic pollutants from water environments.

Refractory organic pollutants cannot be effectively degraded and mineralized by using the conventional biological, physical and chemical wastewater treatment methods. Compared to these traditional technologies, advanced oxidation processes (AOPs) have many advantages with regards to degrading refractory organic pollutants, which include complete mineralization and oxidation of refractory organic pollutants, low secondary pollution outcomes, and small working area. AOPs such as heterogeneous catalysis,[2] photoelectrocatalysis (PEC),[3] photocatalysis,[4] Fenton[5] and Fenton-like,[6] electro-Fenton and photoelectro-Fenton,[7] electrochemical oxidation,[8] *etc.* can be used for wastewater treatment. The PEC technology combines photocatalysis and electrochemical methods, which is an efficient process to remove recalcitrant organic pollutants from water.[9] Biasing the semiconductor photoanode with a voltage under illumination, photogenerated h^+–e^- pairs can be effectively inhibited by an external electric field, resulting in improved photocatalytic activities.[10] A lot of research has been done on the photoanode materials, reaction mechanisms and kinetics of PEC,[11] which shows that it is a promising wastewater treatment technology.

TiO_2 is considered as a promising photocatalyst for wastewater treatment[12] due to its unique photoelectric performance and high photochemical stability, and it has been widely exploited as photoanode material in PEC systems.[13] However, due to the large forbidden bandwidth of TiO_2 (3.2 eV for anatase type), it can only absorb ultraviolet light ($\lambda \leq 387$ nm), which limits its photocatalytic activity under visible light.[14] In addition, photogenerated hole–electron pairs (h^+–e^-) of TiO_2 can rapidly recombine, resulting in low catalytic efficiency.[15] So there have been many attempts to modify titanium dioxide (*e.g.* dye sensitization, metal/non-metal doping, morphology control, and composite photocatalysts) to overcome aforesaid challenges.[16] Among the composite photocatalysts, magnetic

School of Municipal and Environmental Engineering, Shandong Jianzhu University, Jinan 250101, Shandong, China. E-mail: ch1889l@sdjzu.edu.cn

† Electronic supplementary information (ESI) available. See DOI: https://doi.org/10.1039/d2ra05183d

TiO_2 is not only to be separated and recovered from reaction mixtures easily, but also contains some magnetic nanoparticles that have good visible-light absorption and excellent optical/electrical properties, further improving the degradation kinetics of pollutants.[17] Due to its low toxicity, biocompatibility, and superparamagnetism, magnetite (Fe_3O_4) has become one of the most widely used magnetic nanoparticles[18,19] in the fabrication of magnetic TiO_2 photocatalysts. Previous studies have shown that direct contact of the magnetic core with photocatalysts leads to photodissolution of Fe_3O_4,[20] as well as increases recombination of photogenerated charge carriers, thereby reducing the catalytic activity.[21] It has been reported that the SiO_2 interlayer between TiO_2 and the magnetic core can effectively prevent the chemical- and photo-dissolution of Fe_3O_4 [22,23] and can improve the photocatalytic activity of TiO_2.[24] And because of silica's well-known special characteristics, such as low cost, thermal and mechanical stability, surface chemical and adsorption capacity, and optical transparency in the wavelength region where TiO_2 absorbs,[25] previous studies have shown that the core–shell SiO_2@TiO_2 has excellent photocatalytic efficiency for the pollutant degradation than pure TiO_2.[26] In recent years, the research on magnetic TiO_2 composite photocatalysts based on Fe_3O_4 has mostly focused on the application of Fe_3O_4@SiO_2@TiO_2 in photocatalysis.[27–33] The role of Fe_3O_4 in these studies is primarily in the area of magnetic separation, but less attention is paid to how to improve TiO_2 photocatalytic activity. Meanwhile, less research has been conducted on Fe_3O_4@SiO_2@TiO_2 in photoelectrocatalysis,[34] and few studies have comprehensively discussed the issues of expanding the light absorption range, increasing the photoelectrocatalytic activity, effective charge separation performance, and stable recyclability.[35] Therefore, it is necessary to further study the effect of Fe_3O_4 on the band gap and optical absorption of Fe_3O_4@SiO_2@TiO_2 composites, and on the optical and electrical properties of composite photoanodes. We successfully prepared a novel composite photoelectrocatalytic material (Fe_3O_4@SiO_2@-mesoporous TiO_2, FST), encapsulated by layers of Fe_3O_4, SiO_2 and mesoporous TiO_2 particles with a unique core–shell structure. The dense SiO_2 layer prevents the magnetic core from interacting with TiO_2, reducing the electron–hole recombination rate, and preventing photo-dissolution of Fe_3O_4 (ref. [36]) and dissolution under acidic conditions. Fe_3O_4 can lower the band gap of FST and enhance the visible-light absorption. Due to the mesoporous structure and anatase TiO_2 particles, FST has a high specific surface area and exceptional catalytic performance.

Because of mass transfer limitations and the low number of active radicals generated in the heterogeneous PEC systems, the efficiency of photoelectrocatalytic oxidation for pollutant removal should be increased. UV/H_2O_2 systems have been applied to the degradation of various pollutants.[37] The addition of H_2O_2 to other AOPs can improve the degradation efficiency of organic pollutants by strengthening the generation of radicals in a wider spectral range.[38] It has been reported that H_2O_2 can enhance the generation of radicals and improve the degradation efficiency in PEC systems.[39,40]

In this study, a PEC/H_2O_2 coupling system with magnetic FST-loaded photoanode was constructed to discuss the synergistic degradation of organic pollutants. The FST PEC/H_2O_2 system was effective for the degradation of methylene blue, rhodamine B, methyl Orange, and amoxicillin under visible light. With the addition of 2.25% H_2O_2, the reaction kinetic rate constant of the PEC/H_2O_2 synergistic system was nearly 53 times that of individual PEC. In the PEC/H_2O_2 process, $^{\bullet}O_2^-$ and $^{\bullet}OH$ were generated to degrade pollutants, and at the same time, the photogenerated e^- could be captured by a sufficient amount of H_2O_2 to generate $^{\bullet}OH$, which increased the amounts of strong oxidizing substances and promoted the separation of photogenerated h^+–e^-. The formed photocatalytic-electro-H_2O_2 coupling system improved the degradation efficiency of diverse organic pollutants, and maintained the high degradation efficiency within 8 degradation cycles.

2. Experimental section

2.1. Materials and reagents

Indium tin oxide (ITO) coated glass slides (25 mm × 25 mm × 1.1 mm, 8–12 Ω sq^{-1}) were purchased from Sigma-Aldrich (Shanghai Warehouse). Methylene blue (MB, $C_{16}H_{18}ClN_3S$, ≥98%), rhodamine B (Rh B, $C_{28}H_{31}ClN_2O_3$, ≥99%), methyl orange (MO, $C_{14}H_{14}N_3NaO_3S$, 98%), amoxicillin (AMX, $C_{16}H_{19}N_3O_5S\cdot 3H_2O$, 98%), titanium butoxide ($C_{16}H_{36}O_4Ti$, AR), poly(propylene glycol) (PPG 1000, $H[OCH(CH_3)CH_2]_nOH$, average M_n ~ 1000), tetraethyl orthosilicate (TEOS, $C_8H_{20}O_4Si$, >99%), ethanol (CH_3CH_2OH, ≥99.5%) were purchased from Macklin Inc. (Shanghai, China). $FeCl_3\cdot 6H_2O$ (AR), $FeSO_4\cdot 7H_2O$ (AR), NH_3 H_2O (AR, 28%), HCl (AR, 36%), glacial acetic acid (CH_3COOH, AR), and other inorganic metal salts were purchased from Sinopharm Chemical Reagent Co., Ltd (Shanghai, China). All solutions were prepared using ultrapure water from a Milli-Q water purification system (resistivity > 16 MΩ cm at 25 °C).

2.2. Fabrication of photoelectrode

The detailed synthesis of FST and TiO_2 can be found from ESI.†

FST-loaded photoelectrode: 30 mg FST was sonicated in 1 mL ethanol to obtain a 30 mg mL^{-1} FST suspension. The ITO coated glass slides, which have been cleaned *via* ultrasonic waves in acetone, ethanol and distilled water, were connected to a section of electrode wires with conductive silver glue. The epoxy resin glue was used to seal the connection between ITO and the electrode wire. Then, 30 mg mL^{-1} FST suspension was applied on the ITO work surface and dried at 25 °C. During the PEC/H_2O_2 synergistic degradation experiment, the Nd–Fe–B (25 mm × 25 mm × 5 mm) magnet was coated with a layer of polyvinyl chloride film to avoid the contact of the Nd–Fe–B magnet with the reaction solution, and glued to the back of the ITO work surface.[31]

TiO_2-loaded photoelectrode: 30 mg TiO_2 was sonicated in 1 mL ethanol to obtain a 30 mg mL^{-1} TiO_2 suspension. Add the

TiO_2 suspension dropwise to the cleaned ITO conductive surface and dry at 25 °C.

2.3. Characterization of FST

Sample microscopic morphologies were investigated by field emission transmission electron microscopy (JEM-2100F, JEOL, Japan). The X-ray diffraction (XRD) pattern was measured by a BrukerX-ray diffractometer (D8 advance, Germany). X-ray photoelectron spectroscopy (XPS, ThermoEscalab 250Xi, Thermo fisher, USA) was performed to assess surface properties and composition. The UV-vis diffuse reflectance spectrum was determined by UV-visible-near infrared light spectrophotometry (Cary 5000, Agilent, USA). Mesoporous structures of catalysts were measured using the surface area and pore size analyzer (Autosorb-iQ, Quantachrome, USA). Magnetic data was obtained by an MPMS magnetic measurement system (MPMS-VSM, Quantum Design, USA).

2.4. The PEC/H_2O_2 synergistic degradation experiment

Experiments were conducted in a quartz photoelectric reactor with the volume of 60 mL, and the light source was a xenon light source (H8X-F300, Beijing Newbit Technology Co., Ltd.). Potentiostat experiments were performed using a three electrode system consisting of a working electrode (W.E., FST + ITO photoelectrode, anode), a counter electrode (C.E., Pt electrode, cathode), and a reference electrode (R.E., saturated calomel electrode, recorded as SCE), which were controlled using a CHI electrochemical analyzer (CHI 760E, CH Instruments, Inc., USA). The distance between the working electrode and the light source was 10 cm. To enhance conductivity, 0.05 mol per L Na_2SO_4 was added to the pollutants solution (the concentration was 10 mg L^{-1}) as the supporting electrolyte.

The UV-vis spectrophotometer (UV-5800, Shanghai) was used to determine pollutant concentrations ($\lambda_{max,MB}$ = 664 nm, $\lambda_{max,Rh\ B}$ = 554 nm, $\lambda_{max,MO}$ = 463 nm, $\lambda_{max,AMX}$ = 198 nm). The total organic carbon (TOC) was determined using a TOC analyzer (Elementer, vario TOC).

3. Results and discussion

3.1. Morphology and structural analysis of catalysts

The FST microspheres were characterized by scanning transmission electron microscopy (STEM). The high-angle annular dark-field (HAADF) image in Fig. 1a exhibited an overlay of Fe_3O_4 core and TiO_2 shell with a clear separation. A clear contrast difference was also observed in EDS mappings (Fig. 1b), confirming the core–shell structure of FST. The diameter of Fe_3O_4 core was about 580 nm, while thickness of the SiO_2 intermediate layer and TiO_2 shell layer was about 45 nm and 50 nm, respectively.

FST, Fe_3O_4@SiO_2 and Fe_3O_4 nanoparticles were analyzed by X-ray diffraction (XRD) (Fig. 2). Fe_3O_4 nanoparticles exhibited characteristic peaks at 2θ = 30.1°, 35.44°, 43.2°, 53.56°, 57.1° and 62.6°, in agreement with previously reported XRD patterns of Fe_3O_4.[41] The obtained material was Fe_3O_4 crystal with anregular octahedral inverse spinel structure. Fe_3O_4@SiO_2 particles exhibited comparable XRD patterns to Fe_3O_4, indicating that the Fe_3O_4 crystal structure was well maintained. Characteristic peaks at 25.4°, 37.8°, 48.1°, 54.1°, 55.2°, 62.8° and 68.8° of FST can be attributed to anatase TiO_2 (101), (004), (200), (105), (211), (204) and (116), respectively. The high crystallinity of nano-TiO_2 can reduce the migration distance of photogenerated charges, and accordingly reduce the recombination rate.[42]

The characterization data and analysis details of mesoporous structure, magnetic response and XPS spectrum were described in the ESI.†

3.2. Photo-electric performance

The UV-vis diffuse reflectance spectra (DRS) of Fe_3O_4, Fe_3O_4@-SiO_2, TiO_2 nanoparticles and FST were shown in Fig. 3a. TiO_2 exhibited a lower optical absorption response from 400–1000 nm. Comparing the optical absorption responses of Fe_3O_4, Fe_3O_4@SiO_2 and FST at 400–1000 nm, Fe_3O_4 has the strongest light absorption, while FST has a weaker light absorption due to the encapsulation of SiO_2 and TiO_2. However, the visible-NIR absorption of FST is still significantly enhanced compared

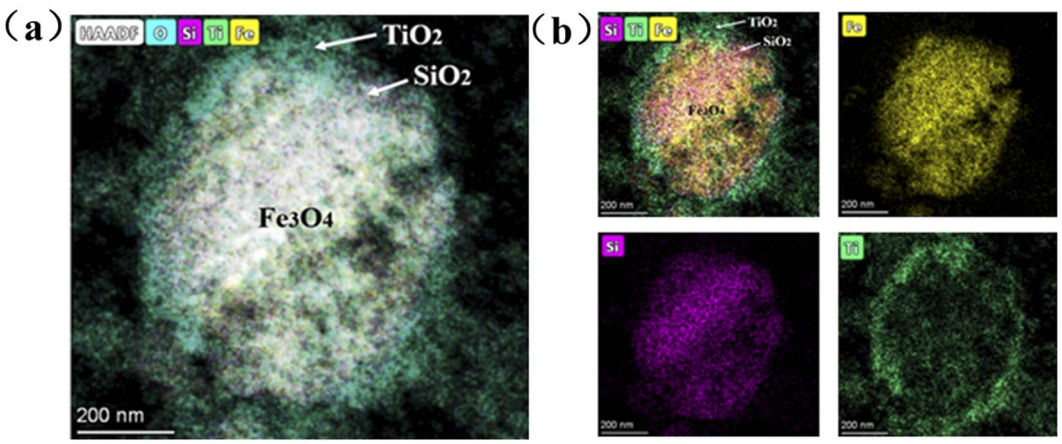

Fig. 1 Scanning transmission electron microscopy (STEM) of FST: (a) HAADF image, (b) EDS mappings of Fe_3O_4, SiO_2, and TiO_2.

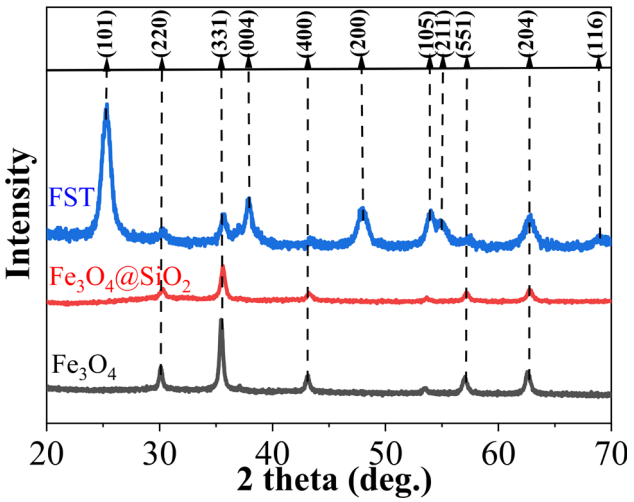

Fig. 2 X-ray diffraction (XRD) pattern.

with that of TiO_2. Since FST is very sensitive to visible light, it enhances the performance of visible-light driven photoelectrocatalytic systems. Using the Tauc equation (eqn (1)) and the Kubelka–Munk function (eqn (2)), band gaps of Fe_3O_4, Fe_3O_4@SiO_2, TiO_2 and FST were calculated as previously reported.[43]

$$[F(R)h\upsilon]^{0.5} = A(h\upsilon - E_g) \quad (1)$$

$$F(R)=(1 - R)^2/2R \quad (2)$$

Fig. 3b shows that the effective E_g values of samples were calculated by plotting $[F(R)h\upsilon]^{0.5}$ *versus* $h\upsilon$. The indirect E_g values of catalysts can be determined by extrapolating the linear part at $[F(R)h\upsilon]^{0.5} = 0$. The E_g values for Fe_3O_4, Fe_3O_4@SiO_2, FST and TiO_2 were 1.49, 1.77, 1.88 and 3.19 eV, respectively. The addition of Fe_3O_4 and SiO_2 reduced the forbidden bandwidth of TiO_2, so that the light absorption of FST extended to the visible light region. The higher photocatalytic performance at higher wavelength has shown the capability to potentially utilize natural solar light as activation source.[29] Compared with other materials (WO_3, ZnO, CdS, *etc.*) with low E_g and activity in visible light, FST has lower E_g, and has the characteristics of nontoxicity, biochemical inertness, low cost of TiO_2.

To investigate the charge transfer of interface between photocatalysts and reaction solutions, Electrochemical Impedance Spectroscopy (EIS) was conducted. The EIS Nyquist plots were shown in Fig. 4a. The circular radius of ITO + FST was smaller than the pristine ITO and ITO + TiO_2. A smaller impedance arc radius at low frequencies signifies a lower charge transfer resistance (R_{ct}),[44] thus, h^+–e^- pairs are efficiently separated. In this regard, ITO + FST possessed faster charge transfer rate and more efficient separation of h^+–e^- pairs than ITO and ITO + TiO_2 at the solid–liquid interface.

The photocurrent of W.E. at +0.6 V (*vs.* SCE) was measured to test the separation efficiency of photogenerated charge by several on/off cycles of visible-light. Photocurrent response curves of pristine ITO, ITO + TiO_2 and ITO + FST were shown in Fig. 4b. The photocurrents generated by ITO + FST, ITO and ITO + TiO_2 photoelectrodes were 0.17, 0.10, and 0.07 mA, respectively. The photocurrent of the ITO + FST electrode was about 1.7-fold that of ITO electrode, and 2.4-fold that of ITO + TiO_2 electrode, respectively. The photocurrent enhancement of ITO + FST induced by visible light indicates that the photogenerated h^+–e^- pairs at the interface have higher separation efficiency and less recombination. The high separation rate of h^+–e^- pairs can promote the movement and subsequent reaction of electrons. However, TiO_2 had lower conductivity than ITO, and absorbed less visible-light, so the photocurrent of the ITO + TiO_2 was lower than that of the pristine ITO.

3.3. Control experiments for different degradation methods

Taking MB as the model pollutant, the effects of direct photolysis (PO), photocatalysis (PC), electrocatalysis (EC), photoelectrocatalysis (PEC), and PEC/H_2O_2 synergistic system on MB degradation were compared (Fig. 5). In the PO, PC, PEC, and PEC/H_2O_2 synergistic system, illumination was the visible light provided by the xenon lamp light source. In the EC, PEC, and

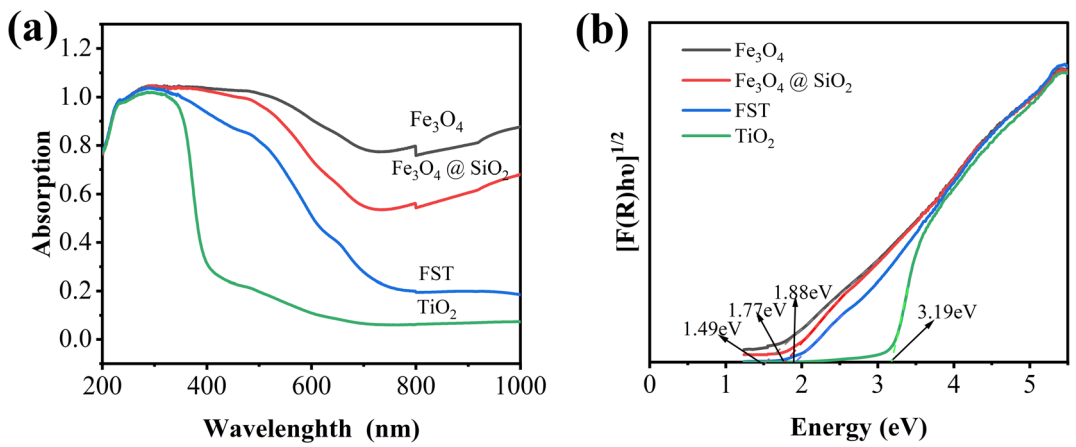

Fig. 3 (a) UV-vis diffuse reflectance spectrum (DRS), (b) Tauc plot of DRS.

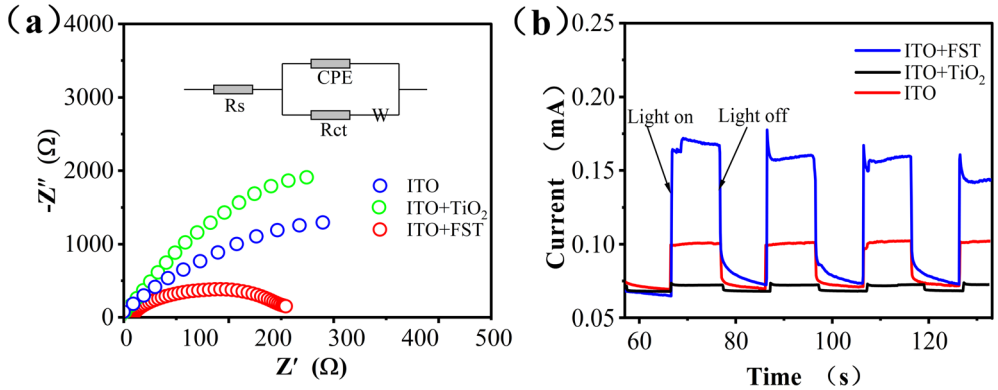

Fig. 4 (a) EIS responses of ITO, ITO + TiO_2 and ITO + FST, (b) surface photocurrent curves.

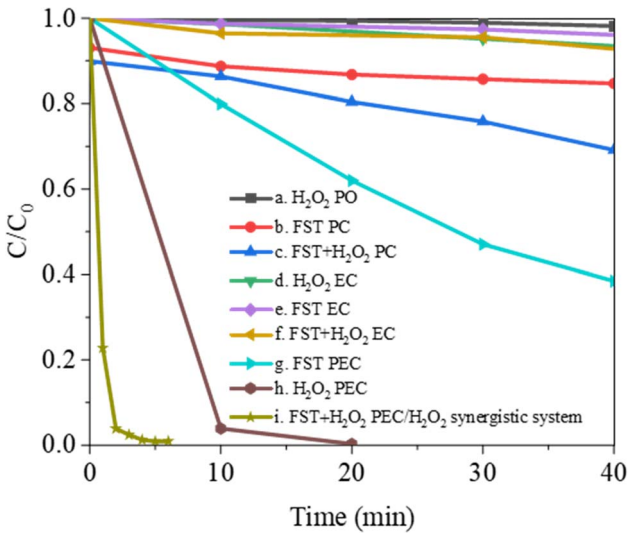

Fig. 5 MB degradation by photolysis (PO), photocatalysis (PC), electrocatalysis (EC), photoelectrocatalysis (PEC), and PEC/H_2O_2 synergistic system.

PEC/H_2O_2 synergistic system, anode potential was +0.6 V (*vs.* SCE). As shown in curve (a), the MB solution showed less than 1.9% degradation when irradiated with visible light in the H_2O_2 PO for 40 min. Curve (b) showed that the degradation efficiency was slightly increased up to about 25% by visible-light PC after adding FST to the MB solution. Curve (c) represented the PC in the presence of H_2O_2, the degradation efficiency was significantly improved, and 31.1% of the MB was removed after 40 min. Curve (d–f) showed the experimental results under EC conditions. MB exhibited stability, whether H_2O_2 (curve (d)) or FST (curve (e)) are added alone. After adding H_2O_2 and FST at the same time (curve (f)), the removal rate slightly increased, while the degradation efficiency was less than 10% after 40 min. Curves (g) and (h) represented experimental results in PEC. Under these conditions, the removal rate of MB reached 61.5% after adding only FST for 40 min, the removal rate of MB reached 96.1% after adding only H_2O_2 for 10 min, and was close to 100% after 20 min. Curve (i) showed the experimental results under PEC/H_2O_2 synergistic degradation conditions. FST and H_2O_2 significantly improved MB degradation when they coexisted, the degradation efficiency was close to 100% after 5 min. Therefore, FST PEC has good synergistic effects with H_2O_2 PO and can quickly remove pollutants.

The synergy factor (S) obtained from eqn (3) [45] elucidates on the synergy between PEC and H_2O_2 photolysis in the PEC/H_2O_2 degradation system, and demonstrates the priority of the combined process.

$$S = K_{12}/(K_1 + K_2) \quad (3)$$

where, K_1, K_2, and K_{12} are kinetic constants for H_2O_2 PO, PEC process, and PEC/H_2O_2 synergistic system, respectively. Experimental data was fitted with the Langmuir–Hinshelwood model, and kinetic constants (Table 1) of the different degradation methods presented by the different curves (a, g, i) in Fig. 5 were calculated. Since the concentration of MB was low, it was assumed that the reaction would take place with a pseudo-first-order equation. The correlation coefficient (R^2) for all processes was above 0.95, indicating that the assumption was reasonable. Based on Table 1, the kinetic constant K of the FST PEC/H_2O_2 synergic system (1.2924 min^{-1}) was found to be about 1436 and 53 times higher than that of the H_2O_2 PO (0.0009 min^{-1}) and FST PEC (0.0244 min^{-1}), respectively. Substituting K_1, K_2 and K_{12} into eqn (3), the value of S was 51.08 (much greater than 1), indicating that the composite process was not a simple addition of PEC and H_2O_2 photolysis.

3.4. Optimization of FST PEC/H_2O_2 synergistic system

Using methylene blue (MB) as the model pollutant, the experimental conditions and degradation performance of the PEC/H_2O_2 synergistic system was studied.

Effects of pH. To study the effects of the pH on MB degradation efficiency, the initial pH of the reaction solution, including 10 mg L^{-1} MB, 0.05 mol per L Na_2SO_4, and 2.25% H_2O_2, was adjusted to 1.0, 2.0, 3.0, 4.0, and 5.0, respectively, and the ITO + FST working electrode (fixed FST 30 mg) was applied at +0.6 V (*vs.* SCE) potential, after which degradation was performed by visible-light irradiation. MB degradation rates under different degradation times in each group were compared and analyzed (Fig. 6a). When pH was in the range of 1.0–5.0, the

Table 1 Kinetic constants and correlation coefficients (R^2) of MB degradation

Curve in Fig. 5	Degradation system	Kinetic constant (min^{-1})	R^2
a	H_2O_2 PO	0.0009 (K_1)	0.9620
g	FST PEC	0.0244 (K_2)	0.9979
i	FST + H_2O_2 PEC/H_2O_2 synergistic system	1.2924 (K_{12})	0.9562

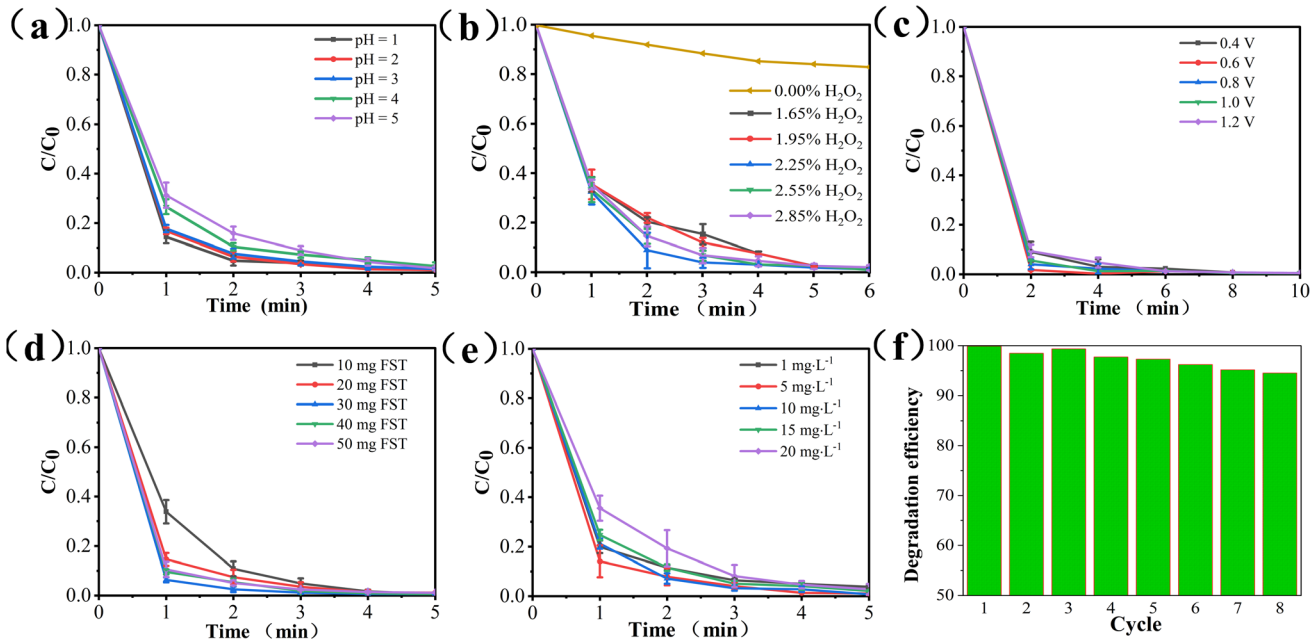

Fig. 6 PEC/H_2O_2 synergistic degradation of MB. (a) pH values, (b) H_2O_2 concentration, (c) anodic potential, (d) FST fixation amount, (e) initial mass concentration of MB, (f) recycling test of FST.

degradation efficiency of MB reached 99% after 6 min. At the pH range of 1.0–3.0, the degradation efficiency was more than 80% after 1 min, and reduced to less than 80% at the pH range of 4.0–5.0, indicating that lower pH value is more conducive for improving photocatalytic activities.[46] The degradation efficiency was largest at pH 1.0, but its advantages relative to pH 2.0–3.0 were not marked. Therefore, pH 3.0 was selected as the optimal reaction pH value.

Effects of H_2O_2 concentrations. To determine the impact of H_2O_2 concentrations on PEC/H_2O_2 synergistic degradation, the ITO + FST working electrode (fixed FST 30 mg) was applied at a bias voltage of +0.6 V (*vs.* SCE). The solution in the photocell contained 10 mg L^{-1} MB, 0.05 mol per L Na_2SO_4, and H_2O_2 with concentrations of 0.00%, 1.65%, 1.95%, 2.25%, 2.55% and 2.85%, respectively. Finally, the solution was adjusted to pH value of 3.0. Degradation efficiency of MB at different degradation times under each group were compared and analyzed (Fig. 6b). The amount of H_2O_2 was established to be an important factor in MB degradation. When H_2O_2 concentration was 2.25%, degradation efficiency was highest within 1 to 3 min. H_2O_2 is beneficial for photocatalytic reaction by trapping the conduction band e^- in order to generate more $^{\cdot}OH$ radicals.[47] However, when the concentration of H_2O_2 was higher than 2.25%, the degradation efficiency of MB didn't continue to increase (2.55% H_2O_2), but decreased (2.85% H_2O_2). Excess H_2O_2 consumes $^{\cdot}OH$, the main active species for degrading MB, and H_2O_2 reacts with $^{\cdot}OH$ to generate $^{\cdot}HO_2$ or $^{\cdot}O_2^-$ with much less reactivity,[48] which reduces the catalytic reaction rate and is unfavorable for MB degradation. Therefore, the optimal concentration of H_2O_2 in this system is 2.25%.

Effects of applied anodic potential. To examine the effects of various W.E. anodic potentials on degradation of MB, 10 mg L^{-1} MB, 0.05 mol per L Na_2SO_4, and 2.25% H_2O_2 were added to the photoelectric reaction cell, the solution pH was adjusted to 3.0, and ITO + FST W.E. (fixed FST 30 mg) was applied at potentials of +0.4 V, +0.6 V, +0.8 V, +1.0 V, and +1.2 V (*vs.* SCE). As shown in Fig. 6c, MB rapidly degraded with increasing potential at the potential range of +0.4–+0.6 V (*vs.* SCE). At the potential of +0.6 V (*vs.* SCE), the degradation efficiency of MB was 98.25% within 2 min. The bias voltage applied on W.E. makes the visible-light photogenerated electrons to flow to the C.E. along the external circuit, thereby reacting with H_2O_2 to generate $^{\cdot}OH$.[49] However, as the potential continued to rise, degradation efficiency of MB decreased, because too high potential caused the electropolymerization of MB[50] and the oxidation of H_2O_2. H_2O_2 had an oxidation peak at +0.6 V (*vs.* SCE) (Fig. S4†). If the

potential exceeded + 0.6 V, the H_2O_2 added in the system was consumed by oxidation, which reduced the MB's degradation efficiency. Thus, anode potential +0.6 V (*vs.* SCE) is the optimal potential of the system.

Effects of FST loading amounts. The fixed amount of FST catalyst on the working electrode directly affects the degradation efficiency of MB. As displayed in Fig. 6d, the effects of FST loading amounts on MB degradation, where the conditions included 10 mg L^{-1} MB, 0.05 mol per L Na_2SO_4, 2.25% H_2O_2, pH 3.0, +0.6 V (*vs.* SCE) to the W.E. and different FST fixed quantities (10, 20, 30, 40, and 50 mg). When the fixed amounts of FST were 10–30 mg, the degradation efficiency of MB increased with increasing fixed amounts of catalysts. When the fixed amount of catalysts was 30 mg, the MB degradation efficiency was maximum, while the degradation efficiency of MB gradually decreased at >30 mg. Too much catalysts negatively affect the degradation efficiency, while agglomeration between catalyst particles reduces the number of active sites.[51] Besides, too much FST increases the thickness of the catalyst layer on the surface of ITO, which affects photoanode conductivity and visible light transmittance. Thus, the optimal fixed amount of FST is determined to be 30 mg.

Effects of MB initial mass concentrations. The effects of MB initial mass concentrations (1, 5, 10, 15, 20 mg L^{-1}) on degradation rates were evaluated. The system contained 0.05 mol per L Na_2SO_4, 2.25% H_2O_2, pH 3.0, the W.E. (fixed FST 30 mg) applied at the potential of +0.6 V (*vs.* SCE). The effects of initial mass concentration of MB solution on degradation were shown in Fig. 6e. The degradation efficiencies of five different concentrations of MB by FST PEC/H_2O_2 system were above 90%, with 10 mg L^{-1} exhibiting the best degradation effect.

Recyclability performance of FST. The PEC/H_2O_2 degradation experiment was performed at optimal conditions of 10 mg L^{-1} MB, 0.05 mol per L Na_2SO_4, 2.25% H_2O_2, pH 3.0, and +0.6 V (*vs.* SCE) potential to the W.E. (fixed FST 30 mg). After W.E. was vacuum-dried at 80 °C, the above degradation experiment was repeated 8 times, and then the degradation efficiency of MB measured each time. As can be seen from Fig. 6f, the MB degradation efficiency were above 98% within 5 recycled and reused experiments, and the degradation efficiency only showed a slight decrease in 6–8 degradation cycles, demonstrating that FST catalysts were recyclable and stable. Comparable findings have been reported, where such magnetically attached FST working electrode had the desired stability.[33] The magnetic FST was loaded on the surface of ITO working electrode by attractive forces of the magnet, the FST was firmly fixed and had a good stability.

3.5. PEC/H_2O_2 synergistic degradation of pollutants

To further discussion the versatility of PEC/H_2O_2 synergistic system for the treatment of different organic pollutants, the degradation experiments of four kinds of pollutants (MB, Rh B, MO, AMX) were carried out. As displayed in Fig. 7, the maximum degradation efficiencies of MB, Rh B, MO, and AMX in the FST PEC/H_2O_2 synergistic system could reach up to 98.8%, 96.7%, 97.7% and 83.9% after 8 min illumination,

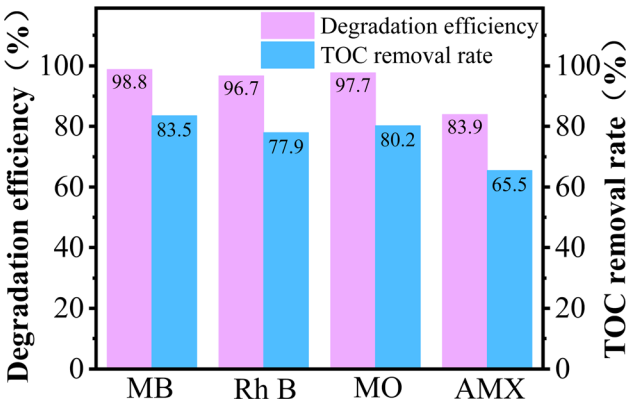

Fig. 7 Degradation efficiency and TOC removal rate of MB, Rh B, MO, and AMX.

respectively. Moreover, this system obtained TOC removal rate of 83.5% (MB), 77.9% (Rh B), 80.2% (MO), and 65.5% (AMX), indicating the incomplete mineralization of MB, Rh B, MO, and AMX in the PEC/H_2O_2 system within 8 min and the presence of intermediate products. In general, the FST PEC/H_2O_2 synergistic degradation system showed excellent oxidative degradation and mineralization abilities for MB, Rh B, MO, and AMX, indicating the wide applicability of PEC/H_2O_2 coupling system for organic pollutants wastewater treatment.

3.6. Degradation mechanism

The possible reaction mechanism of the FST PEC/H_2O_2 synergistic degradation system is shown in Fig. 8. When visible light irradiates FST, the energy ($h\nu$) of the incident photon is higher than the semiconductor band gap (E_g), and the electrons in the valence band (VB) are excited to transition into the conduction band (CB) to become highly active photogenerated electrons (e^-); photogenerated positively charged holes (h^+) stay in the VB, generating photogenerated h^+–e^- pairs. Upon separation, the e^- and h^+ move to the surface of the semiconductor. The h^+ in the VB reacts with H_2O to generate hydroxyl radicals (eqn (4)); the e^- in the CB moves to the platinum counter electrode through an external circuit under the action of a bias voltage. Photogenerated e^- reacts with adsorbed or dissolved O_2 on the electrode surface to form $^{\cdot}O_2^-$ (eqn (5)). In an acidic environment of the system, e^- reacts with O_2 to form H_2O_2 (eqn (6)),[52,53] after which H_2O_2 reacts with $^{\cdot}O_2^-$ to produce more $^{\cdot}OH$ (eqn (7)).[54] By adding H_2O_2 to the system, e^- can directly activate H_2O_2 to generate a large number of $^{\cdot}OH$ (eqn (8)).[49] The $^{\cdot}OH$ and $^{\cdot}O_2^-$ in the system are involved in oxidative degradation of pollutants.

$$h^+ + H_2O \rightarrow {}^{\cdot}OH + H^+ \quad (4)$$

$$e^- + O_2 \rightarrow {}^{\cdot}O_2^- \quad (5)$$

$$e^- + O_2 + 2H^+ \rightarrow H_2O_2 \quad (6)$$

$$H_2O_2 + {}^{\cdot}O_2^- \rightarrow {}^{\cdot}OH + OH^- + O_2 \quad (7)$$

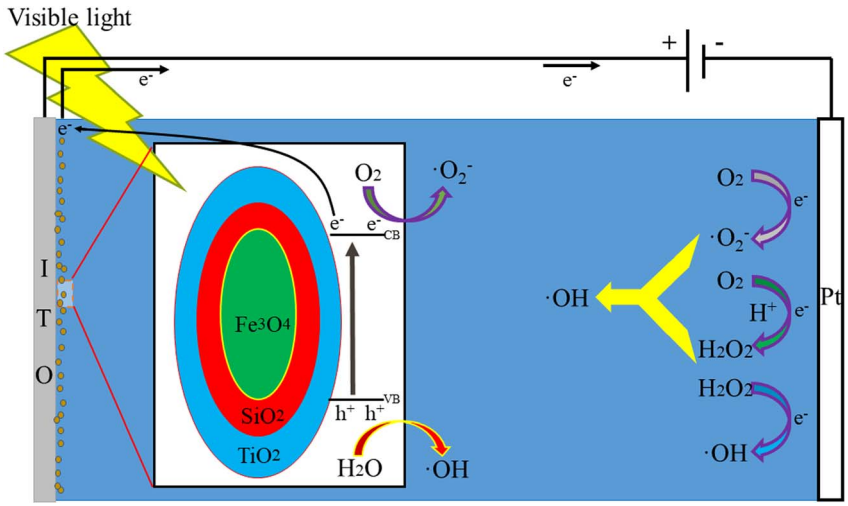

Fig. 8 Reaction mechanism of FST PEC/H_2O_2 synergistic degradation system.

$$H_2O_2 + e^- \rightarrow {}^{\cdot}OH + OH^- \quad (8)$$

The free radical quenching experiment was performed to verify the generation and degradation mechanisms of active free radicals in the PEC/H_2O_2 synergistic degradation reaction. Tert-butanol (TBA), benzoquinone (BQ), ethylenediaminetetraacetic acid disodium salt (EDTA–2Na), and silver nitrate ($AgNO_3$) were respectively added to the FST PEC/H_2O_2 degradation system for MB as quenchers, to scavenge for related reactive species, including hydroxyl radicals ($^{\cdot}OH$), superoxide radicals ($^{\cdot}O_2^-$), photogenerated holes (h^+) and photogenerated electrons (e^-).[55,56] Fig. 9 displayed that addition of TBA, as a scavenger for $^{\cdot}OH$, significantly inhibited the MB degradation reaction, indicating that $^{\cdot}OH$ was the main species in this system. From the eqn (4), (5), (6), (7) and (8), $^{\cdot}OH$ is the most active substance produced by the system. The degradation efficiency of MB slightly decreased after adding BQ, suggesting that variations of $^{\cdot}O_2^-$ had little effects on MB degradation. $^{\cdot}O_2^-$ was only generated by eqn (5), and accounted for a small amount of active species. The addition of EDTA–2Na had no significant effects on MB degradation. Although EDTA–2Na captures h^+ and reduces the $^{\cdot}OH$ generated in eqn (4), the capture of h^+ is more conducive to separating e^- and h^+, and the eqn (5), (6), (7) and (8) caused by photogenerated e^- can still generate large amounts of hydroxyl radicals, which continue to degrade pollutants. When $AgNO_3$ was added as an e^- scavenger, MB undergoed a certain degradation efficiency change, indicating that e^- played one significant role in this system. Eqn (5), (6), (7) and (8) show that e^- contributes to generation $^{\cdot}O_2^-$ and $^{\cdot}OH$. Based on the above findings, the $^{\cdot}OH$ generated by e^- and external H_2O_2 in eqn (8) are the most important active species in the pollutant degradation process. In the FST PEC/H_2O_2 synergistic degradation system, electrons are generated by FST photocatalysis, and bias voltage promotes separation of h^+ and e^-. Due to reactions involving photogenerated h^+ and e^-, $^{\cdot}OH$ and $^{\cdot}O_2^-$ are formed, while electrons promote the formation of $^{\cdot}OH$ from a large amount of H_2O_2 in the solution, forming the photocatalytic-electro-H_2O_2 synergistic system to promote the rapid degradation of pollutants.

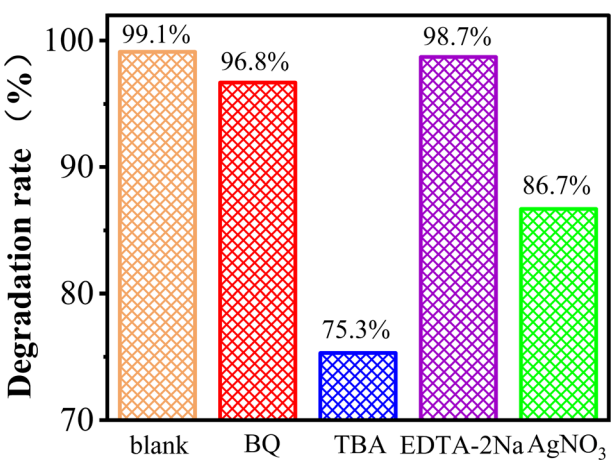

Fig. 9 Degradation efficiency of MB using different radical scavengers.

4. Conclusions

In summary, visible-light driven PEC/H_2O_2 coupling system was developed for degradation of organic pollutants (MB, Rh B, MO, AMX) by magnetic FST-loaded photoelectrode. Through characterization by TEM, XRD, UV-vis DRS, BET, XPS and EIS, the chemical and physical properties of the FST catalyst were systematically analyzed. Taking advantage of the synergistic effect of photoelectrocatalysis and H_2O_2 photolysis, the system exhibited greatly enhanced performance. The FST PEC/H_2O_2 synergistic degradation system showed comparable degradation efficiencies for MB (98.8%), Rh B (96.7%), MO (97.7%), and AMX (83.9%), indicating the wide applicability for various organic pollutants wastewater treatment. In the PEC/H_2O_2 process, through applications of a bias voltage on the working electrode, photogenerated electrons were guided along the

external electric field to the auxiliary electrode, thereby reducing h^+–e^- recombination, realizing the photo-electric coupling effect. At the same time, the photogenerated electrons were captured by a sufficient amount of H_2O_2 in the system to generate $^{\bullet}OH$, which increased the amounts of strong oxidizing substances and facilitated the separation of photogenerated h^+ and e^-. The results of quenching experiments also proved that $^{\bullet}OH$ and $^{\bullet}O_2^-$ were main reactive species in the photocatalytic-electro-H_2O_2 oxidation processes. This work brings new insights to efficiently purify organic pollutants by PEC coupled with peroxide under visible light illumination.

Author contributions

Bo Zhang: investigation, methodology, writing – original draft. Xuemei Li: conceptualization, validation, resources, writing – review & editing, supervision, project administration, funding acquisition. Yongshan Ma: software, visualization. Tianyi Jiang: data curation. Yanyan Zhu: validation. Huixue Ren: supervision, funding acquisition. All authors have approved the final version of the manuscript.

Conflicts of interest

There are no conflicts to declare.

Acknowledgements

This project was financially supported by Natural Science Foundation of Shandong Province (No. ZR2020MD115, ZR2020MB086, ZR202102280483).

References

1 E. Bailón-García, A. Elmouwahidi, M. A. Álvarez, F. Carrasco-Marín, A. F. Pérez-Cadenas and F. J. Maldonado-Hódar, New carbon xerogel-TiO_2 composites with high performance as visible-light photocatalysts for dye mineralization, *Appl. Catal., B*, 2017, **201**, 29–40.

2 P. An, Y. Fu, D. L. Wei, Y. L. Guo, W. C. Zhan and J. S. Zhang, Hollow Nitrogen-Rich Carbon Nanoworms with High Activity for Metal-Free Selective Aerobic Oxidation of Benzyl Alcohol, *Acta Phys.-Chim. Sin.*, 2021, **37**, 2001025.

3 S. Li, W. Xu, L. Meng, W. Tian and L. Li, Recent Progress on Semiconductor Heterojunction-Based Photoanodes for Photoelectrochemical Water Splitting, *Small Sci.*, 2022, **2**, 2100112.

4 Y. Zhang, S. M. Zhao, Q. W. Su and J. L. Xu, Visible light response ZnO–C_3N_4 thin film photocatalyst, *Rare Met.*, 2021, **40**, 96–104.

5 M. Xiao, Y. Qi, Q. Feng, K. Li, K. Fan, T. Huang, P. Qu, H. Gai and H. Song, P-cresol degradation through Fe(III)-EDDS/H_2O_2 Fenton-like reaction enhanced by manganese ion: Effect of pH and reaction mechanism, *Chemosphere*, 2021, **269**, 129436.

6 S. Qu, W. Wang, X. Pan and C. Li, Improving the Fenton catalytic performance of FeOCl using an electron mediator, *J. Hazard. Mater.*, 2020, **384**, 121494.

7 I. Sirés, C. Arias, P. L. Cabot, F. Centellas, J. A. Garrido, R. M. Rodríguez and E. Brillas, Degradation of clofibric acid in acidic aqueous medium by electro-Fenton and photoelectro-Fenton, *Chemosphere*, 2007, **66**, 1660–1669.

8 S. Periyasamy, X. Lin, S. O. Ganiyu, S. Kamaraj, A. Thiam and D. Liu, Insight into BDD electrochemical oxidation of florfenicol in water: kinetics, reaction mechanism, and toxicity, *Chemosphere*, 2022, **288**, 132433.

9 R. Wang, J. Bai, Y. Li, Q. Zeng, J. Li and B. Zhou, $BiVO_4$/$TiO_2(N_2)$ Nanotubes Heterojunction Photoanode for Highly Efficient Photoelectrocatalytic Applications, *Nano-Micro Lett.*, 2016, **9**, 14.

10 S. Wu and Y. H. Hu, A comprehensive review on catalysts for electrocatalytic and photoelectrocatalytic degradation of antibiotics, *Chem. Eng. J.*, 2021, **409**, 127739.

11 P. Alulema-Pullupaxi, P. J. Espinoza-Montero, C. Sigcha-Pallo, R. Vargas and J. L. Paz, Fundamentals and Applications of Photoelectrocatalysis as an Efficient Process to Remove Pollutants from Water: A Review, *Chemosphere*, 2021, **281**, 130821.

12 J. Schneider, M. Matsuoka, M. Takeuchi, J. Zhang, Y. Horiuchi, M. Anpo and D. W. Bahnemann, Understanding TiO_2 photocatalysis: mechanisms and materials, *Chem. Rev.*, 2014, **114**, 9919–9986.

13 Y. Z. Wang, M. Zu, X. S. Zhou, H. Lin, F. Peng and S. Q. Zhang, Designing efficient TiO_2-based photoelectrocatalysis systems for chemical engineering and sensing, *Chem. Eng. J.*, 2020, **381**, 122605.

14 Y. Li, D. D. Cheng, Y. Luo and L. X. Yang, Coaxial Fe_2O_3/TiO_2 nanotubes for enhanced photo-Fenton degradation of electron-deficient organic contaminant, *Rare Met.*, 2021, **40**, 3543–3553.

15 C. Zhai, M. Zhu, Y. Lu, F. Ren, C. Wang, Y. Du and P. Yang, Reduced graphene oxide modified highly ordered TiO_2 nanotube arrays photoelectrode with enhanced photoelectrocatalytic performance under visible-light irradiation, *Phys. Chem. Chem. Phys.*, 2014, **16**, 14800–14807.

16 Z. Q. Long, Q. G. Li, T. Wei, G. M. Zhang and Z. J. Ren, Historical development and prospects of photocatalysts for pollutant removal in water, *J. Hazard. Mater.*, 2020, **395**, 122599.

17 G. Mamba and A. Mishra, Advances in Magnetically Separable Photocatalysts: Smart, Recyclable Materials for Water Pollution Mitigation, *Catalysts*, 2016, **6**, 79.

18 W. J. Zhou, X. R. Xiao, Y. H. Liu and X. Zhang, Magnetic Se/Fe/PCN-Catalyzed Oxidative Cracking Alkenes in O_2, *Chin. J. Org. Chem.*, 2022, **42**, 1849–1855.

19 X. Y. Chen, J. F. Mao, C. Liu, C. Chen, H. E. Cao and L. Yu, An unexpected generation of magnetically separable Se/Fe_3O_4 for catalytic degradation of polyene contaminants with molecular oxygen, *Chin. Chem. Lett.*, 2020, **31**, 3205–3208.

20 D. Beydoun, R. Amal, G. Low and S. Mcevoy, Occurrence and prevention of photodissolution at the phase junction of

magnetite and titanium dioxide, *J. Mol. Catal. A: Chem.*, 2002, **180**, 193–200.

21 S. Xu, W. Shangguan, J. Yuan, M. Chen and J. Shi, Preparations and photocatalytic properties of magnetically separable nitrogen-doped TiO_2 supported on nickel ferrite, *Appl. Catal., B*, 2007, **71**, 177–184.

22 P. M. Álvarez, J. Jaramillo, F. L. Ero and P. K. Plucinski, Preparation and characterization of magnetic TiO_2 nanoparticles and their utilization for the degradation of emerging pollutants in water, *Appl. Catal., B*, 2010, **100**, 338–345.

23 Y. Chi, Q. Yuan, Y. Li, L. Zhao and W. Yan, Magnetically separable Fe_3O_4@SiO_2@TiO_2-Ag microspheres with well-designed nanostructure and enhanced photocatalytic activity, *J. Hazard. Mater.*, 2013, **262**, 404–411.

24 C. Feng, Y. Xie, J. Zhao and G. Lu, Photocatalytic degradation of dyes on a magnetically separated photocatalyst under visible and UV irradiation, *Chemosphere*, 2001, **44**, 1159–1168.

25 S. Kamaruddin and D. Stephan, The preparation of silica-titania core-shell particles and their impact as an alternative material to pure nano-titania photocatalysts, *Catal. Today*, 2011, **161**, 53–58.

26 I. Kitsou, P. Panagopoulos, T. Maggos, M. Arkas and A. Tsetsekou, Development of SiO_2@TiO_2 core-shell nanospheres for catalytic applications, *Appl. Surf. Sci.*, 2018, **441**, 223–231.

27 M. Khan, C. S. L. Fung, A. Kumar, J. He and I. M. C. Lo, Unravelling mechanistic reasons for differences in performance of different Ti- and Bi-based magnetic photocatalysts in photocatalytic degradation of PPCPs, *Sci. Total Environ.*, 2019, **686**, 878–887.

28 A. Kumar, M. Khan, L. Fang and I. M. C. Lo, Visible-light-driven N-TiO_2@SiO_2@Fe_3O_4 magnetic nanophotocatalysts: synthesis, characterization, and photocatalytic degradation of PPCPs, *J. Hazard. Mater.*, 2017, **370**, 108–116.

29 J. He, X. Zeng, S. Lan and I. M. C. Lo, Reusable magnetic Ag/Fe,N-TiO_2@Fe_3O_4@SiO_2 composite for simultaneous photocatalytic disinfection of *E.coli* and degradation of bisphenol A in sewage under visible light, *Chemosphere*, 2018, **217**, 869–878.

30 Q. Y. Li, K. R. Ma, Z. J. Ma, Q. Wei, J. G. Liu, S. P. Cui and Z. R. Nie, Preparation and enhanced photocatalytic performance of a novel photocatalyst: hollow network Fe_3O_4/mesoporous SiO_2/TiO_2 (FST) composite microspheres, *Microporous Mesoporous Mater.*, 2018, **265**, 18–25.

31 J. B. Cai, X. F. Lin and H. F. Zhou, Lysine surface modified Fe_3O_4@SiO_2@TiO_2 microspheres-based preconcentration and photocatalysis for in situ selective determination of nanomolar dissolved organic and inorganic phosphorus in seawater, *Sens. Actuators, B*, 2016, **224**, 48–54.

32 J. Rashid, M. A. Barakat, Y. Ruzmanova and A. Chianese, Fe_3O_4@SiO_2@TiO_2 nanoparticles for photocatalytic degradation of 2-chlorophenol in simulated wastewater, *Environ. Sci. Pollut. Res.*, 2015, **22**, 3149–3157.

33 J. Ma, S. Guo, X. Guo and H. G. Ge, Liquid-phase deposition of TiO_2 nanoparticles on core-shell Fe_3O_4@SiO_2 spheres: preparation, characterization, and photocatalytic activity, *J. Nanopart. Res.*, 2015, **17**, 1–11.

34 X. Hu, J. Yang and J. Zhang, Magnetic loading of TiO_2/SiO_2/Fe_3O_4 nanoparticles on electrode surface for photoelectrocatalytic degradation of diclofenac, *J. Hazard. Mater.*, 2011, **196**, 220–227.

35 J. Su, Y. Zhang, S. Xu, S. Wang, H. Ding and S. Pan, Highly efficient and recyclable triple-shelled Ag@Fe_3O_4@SiO_2@TiO_2 photocatalysts for degradation of organic pollutants and reduction of hexavalent chromium ions, *Nanoscale*, 2014, **6**, 5181–5192.

36 L. Zhang, W. Wang, S. Sun, Y. Sun, E. Gao and Z. Zhang, Elimination of BPA endocrine disruptor by magnetic BiOBr@SiO_2@Fe_3O_4 photocatalyst, *Appl. Catal., B*, 2014, **148–149**, 164–169.

37 K. Bezerra, T. R. Fiaschitello, G. Labuto, H. S. Freeman and S. Costa, Reuse of water from real reactive monochromic and trichromic wastewater for new cotton dyes after efficient treatment using H_2O_2 catalyzed by UV light, *J. Environ. Chem. Eng.*, 2021, **9**, 105731.

38 X. Li, S. Liu, D. Cao, R. Mao and X. Zhao, Synergetic activation of H_2O_2 by photo-generated electrons and cathodic Fenton reaction for enhanced self-driven photoelectrocatalytic degradation of organic pollutants, *Appl. Catal., B*, 2018, **235**, 1–8.

39 P. D. R. A. Paula, R. P. Cavalcante, D. A. Da Silva, L. Silva, T. Silva, F. Gozzi, E. Mcglynn, A. Brady-Boyd, G. A. Casagrande and H. Wender, H_2O_2-assisted photoelectrocatalytic degradation of Mitoxantrone using CuO nanostructured films: Identification of by-products and toxicity, *Sci. Total Environ.*, 2019, **651**, 2845–2856.

40 J. Sun, Y. Guo, Y. Wang and D. Cao, H_2O_2 assisted photoelectrocatalytic degradation of diclofenac sodium at g-C_3N_4/$BiVO_4$ photoanode under visible light irradiation, *Chem. Eng. J.*, 2018, **332**, 312–320.

41 Z. Lei, X. Pang, N. Li, L. Lin and Y. Li, A novel two-step modifying process for preparation of chitosan-coated Fe_3O_4/SiO_2 microspheres, *J. Mater. Process. Technol.*, 2009, **209**, 3218–3225.

42 Q. Zhang, J. B. Joo, Z. Lu and M. Dahl, Self-assembly and photocatalysis of mesoporous TiO_2 nanocrystal clusters, *Nano Res.*, 2011, **4**, 103–114.

43 Y. Ma, J. Cui, M. Yin, X. Li and Y. Liu, Enhancement of visible light driven dye degradation and photocatalytic H_2 evolution over MoS_2 through combination with perylene diimide aggregates, *New J. Chem.*, 2021, **45**, 14432–14443.

44 S. Komtchou, A. Dirany, P. Drogui, D. Robert and P. Lafrance, Removal of atrazine and its by-products from water using electrochemical advanced oxidation processes, *Water Res.*, 2017, **125**, 91–103.

45 P. Qiu, T. Zhao, X. Zhu, B. Thokchom, J. Yang, W. Jiang, L. Wang, Y. Fan, X. Li and W. Luo, A confined micro-reactor with a movable Fe_3O_4 core and a mesoporous TiO_2 shell for a photocatalytic Fenton-like degradation of bisphenol A, *Chin. Chem. Lett.*, 2021, **32**, 1456–1461.

46 A. Li, G. Li, Y. Zheng, L. Feng and Y. Zheng, Photocatalytic Property and Reaction Mechanism of (Ni-Mo)/TiO_2 Nano Thin Film Evaluated with Congo Red, *Acta Phys.-Chim. Sin.*, 2012, **28**, 457–464.

47 M. R. Sohrabi and M. Ghavami, Comparison of direct yellow 12 dye degradation efficiency using UV/semiconductor and UV/H_2O_2/semiconductor systems, *Desalination*, 2010, **252**, 157–162.

48 J. Ma, W. Song, C. Chen, W. Ma, J. Zhao and Y. Tang, Fenton Degradation of Organic Compounds Promoted by Dyes under Visible Irradiation, *Environ. Sci. Technol.*, 2005, **39**, 5810–5815.

49 R. Daghrir, P. Drogui and M. A. El Khakani, Photoelectrocatalytic oxidation of chlortetracycline using Ti/TiO_2 photo-anode with simultaneous H_2O_2 production, *Electrochim. Acta*, 2013, **87**, 18–31.

50 J. Xu, H. Olvera-Vargas, F. Y. H. Teo and O. Lefebvre, A comparison of visible-light photocatalysts for solar photoelectrocatalysis coupled to solar photoelectro-Fenton: application to the degradation of the pesticide simazine, *Chemosphere*, 2021, **276**, 130138.

51 A. Sharma and B. Lee, Integrated ternary nanocomposite of TiO_2/NiO/reduced graphene oxide as a visible light photocatalyst for efficient degradation of o-chlorophenol, *J. Environ. Manage.*, 2016, **181**, 563–573.

52 C. Qu and D. Liang, Novel electrochemical advanced oxidation processes with H_2O_2 generation cathode for water treatment: a review, *J. Environ. Chem. Eng.*, 2022, **10**, 107896.

53 P. J. Espinoza-Montero, P. Alulema-Pullupaxi and B. A. Frontana-Uribe, Electrochemical production of hydrogen peroxide on Boron-Doped diamond (BDD) electrode, *Curr. Opin. Solid State Mater. Sci.*, 2022, **26**, 100988.

54 D. Liu, R. Tian, J. Wang, E. Nie, X. Piao, X. Li and Z. Sun, Photoelectrocatalytic degradation of methylene blue using F doped TiO_2 photoelectrode under visible light irradiation, *Chemosphere*, 2017, **185**, 574–581.

55 F. Chen, Q. Yang, Y. Wang, J. Zhao, D. Wang, X. Li, Z. Guo, H. Wang, Y. Deng, C. Niu and G. Zeng, Novel ternary heterojunction photcocatalyst of Ag nanoparticles and g-C_3N_4 nanosheets co-modified $BiVO_4$ for wider spectrum visible-light photocatalytic degradation of refractory pollutant, *Appl. Catal., B*, 2017, **205**, 133–147.

56 C. Zhou, C. Lai, D. Huang, G. Zeng, C. Zhang, M. Cheng, L. Hu, J. Wan, W. Xiong, M. Wen, X. Wen and L. Qin, Highly porous carbon nitride by supramolecular preassembly of monomers for photocatalytic removal of sulfamethazine under visible light driven, *Appl. Catal., B*, 2018, **220**, 202–210.